Frequency Domain System Identification of a Robinson R44 in Hover

Stefano Geluardi

Project Leader,

Max Planck Institute for Biological Cybernetics,

72076 Tübingen, Germany,

Phone: +49 7071 601 607,

Fax: +49 7071 601 616,

Email: stefano.geluardi@tuebingen.mpg.de.

Frank M. Nieuwenhuizen

Project Leader,

Max Planck Institute for Biological Cybernetics,

72076 Tübingen, Germany.

Joost Venrooij

Project Leader,

Max Planck Institute for Biological Cybernetics,

72076 Tübingen, Germany.

Lorenzo Pollini

Associate Professor,

Università di Pisa,

56126 Pisa, Italy.

Heinrich H. Bülthoff

Professor and Director,

Max Planck Institute for Biological Cybernetics,

72076 Tübingen, Germany.

Abstract

The civil light helicopter domain has not fully benefited yet from the advantages system identification methods can offer. The aim of this paper is to show that system identification methods are mature enough to be successfully implemented in the civil helicopter domain. To achieve this goal, a Robinson R44 Raven II is identified in this work. The identification focuses on the hover trim condition. A lean frequency domain identification method is adopted. Furthermore, a new procedure is proposed to limit the sensitivity of the state-space minimization algorithm to initial parametric values and bounds. The resulting state-space model presents good predictive capabilities and is able to capture high frequency rotor-body dynamics. The model is also validated with the help of a helicopter pilot by performing closed-loop control task maneuvers in the MPI CyberMotion Simulator. The overall validation shows that the implemented model is suitable for handling qualities studies, high frequency control system designs and realistic simulations that involve piloted closed-loop control tasks.

Nomenclature

a_x, a_y, a_z accelerometer components along the body axes (longitudinal, lateral, vertical), $[m/s^2]$

p, q, r fuselage angular rates (roll rate, pitch rate, yaw rate), $[rad/s]$

u, v, w velocity components along the body axes (longitudinal, lateral, vertical), $[m/s]$

x_a, y_a, z_a offset of the accelerometer package relative to the center of gravity, $[m]$

a lift-curve slope, $[1/rad]$

C_0 Carpenter-Fridovich inflow constant

X, Y, Z external forces on the helicopter center of gravity (longitudinal, lateral, vertical), $[N]$

L, M, N external moments about the helicopter center of gravity (roll, pitch, yaw), $[N \cdot m]$

L_p example of dimensional stability derivative; $L_p \equiv \delta L/\delta p$

$L_{\delta_{lat}}$ example of dimensional control derivative; $L_{\delta_{lat}} \equiv \delta L/\delta\delta_{lat}$

R main rotor radius, $[m]$

m helicopter mass, $[kg]$

g gravitational acceleration, $[m/s^2]$

s Laplace transform variable

ϕ, θ, ψ fuselage angular attitude (roll, pitch, yaw) earth-fixed coordinates, $[rad]$

$\beta_0, \beta_{1c}, \beta_{1s}$ rotor coning, longitudinal and lateral flapping angles, $[rad]$

τ_f rotor flap time constant, $[s]$

ν rotor inflow velocity, $[m/s]$

$\bar{\nu}_0$ trim inflow ratio

γ Lock number

ξ, ω damping and natural frequency of a second order system

η_{C_t} integrated perturbation thrust coefficient

σ rotor solidity

ρ atmospheric density, $[Kg/m^3]$

$\delta_{lat}, \delta_{lon}, \delta_{ped}, \delta_{col}$ helicopter control inputs (lateral cyclic, longitudinal cyclic, pedals rudder, collective lever), $[deg]$

Ω rotor rotation speed, $[rad/s]$

ω frequency, $[rad/s]$

Introduction

In the past few decades, system identification studies have significantly contributed to the improvement of existing helicopters and the development of new ones. System identification consists of creating physical system models from measured test data. Nowadays, it is an established routine procedure in the aircraft field as it is used to obtain 3 and 6 Degrees of Freedom (DoF) linearized rigid body models (Ref. 1). Recently, identification methods have also been applied in the rotorcraft field as an alternative to the implementation of non-linear full-flight-envelope models (Ref. 2). This is linked to previous studies that have proven how complex non-linear models have deficiencies at predicting fundamental dynamics like primary roll, vertical response or pitch/roll cross-coupling (Ref. 3). These deficiencies are probably due to the need for nonlinear models to be valid over the full-flight-envelope. Based on these considera-

tions, in 1991 the AGARD Working Group WG 18 on 'Rotorcraft System Identification' investigated how identification theories can be applied to rotorcraft systems. The result was the creation of a large database of flight tests measurements for three different helicopters: the Apache AH-64, the MBB BO-105 and the SA-330 Puma (Ref. 4). The database was then used to apply and validate different frequency and time domain system identification methods. This and similar works on system identification (Ref. 2) have opened a new branch of research focused on understanding helicopter dynamics and developing new control systems for helicopters (Refs. 5, 6). In particular, the military domain has benefited from the knowledge and experience gained from this kind of research (Refs. 7–9). As a result of this, many studies have been conducted on large-scale military helicopters (Refs. 3, 10, 11).

Conversely, the civil light helicopter domain has not fully benefited yet from the advantages system identification methods can offer. System identification techniques presented in literature have important requirements: experienced test pilots able to perform specific maneuvers; a reasonable amount of hours of flight tests to increase the chance of collecting reliable data; the availability of system identification software tools and expert engineers able to build reliable models from the collected data. These requirements make civil helicopter manufacturers skeptical about including system identification studies into the production cycle. Other reasons are the expensive instrumentation technologies that are commonly used in the military domain and the large number of hours required for flight tests (Ref. 12). Therefore, the design of many civil light-weight helicopters largely relies on manual tuning and trial-and-error methods, based on experts' knowledge.

This explains why only few system identification studies have been performed for civil purposes until now. The main body of work involves the research conducted on a MBB BO-105 helicopter to investigate higher order models that can include rotor degrees of freedom (Ref. 13, 14). These studies have been continued on the EC-135 from Airbus Helicopters, operated by the German Aerospace Center (Ref. 15), and currently focus on developing inverse dynamic models to cancel out inherent helicopter dynamics for simulation purposes (Ref. 16). A recent application of system identification methods on civil light helicopters has been the development of a full flight envelope helicopter simulation of the IAI Bell 206, obtained by stitching together dynamic models at different flight conditions (Ref. 17).

If the complexity of the system identification process could be reduced and made less costly, and if the

advantages of its application were clearly demonstrated, the civil helicopter domain could benefit in terms of reduced production cycle costs and improved helicopter safety and reliability.

The goal of this paper is to prove that system identification methods can be successfully applied in the civil domain to obtain reliable helicopter models for handling qualities analyses and control system designs. In this paper, a Robinson R44 Raven II helicopter is considered. The identification is implemented for the hover flight condition. To achieve the proposed goal and overcome the complexity-hurdle that the civil helicopter domain faces, a simplified and lean identification method is adopted.

An important aspect of this procedure is the analysis of the dynamic complexity of the model. A 6 DoF model is generally adequate for handling qualities evaluations. However, higher order model structures are necessary for flight control system design or for model validation studies (Ref. 2). Many works demonstrated that high bandwidth control systems need to include rotor's DoFs. In Ref. 5 a variable-stability CH47 helicopter was used to demonstrate how rotor dynamics and lags in the control system can limit the feedback gains. Later, studies on high-order helicopter models proved that for hingeless single-rotor helicopters the coupled rotor/body-flapping mode can limit the gain on the attitude control feedback, while the lead-lag mode can limit the gain on the attitude-rate control feedback (Ref. 18). Recent studies by DLR in Germany have confirmed the importance of suppressing the air resonance due to the regressive lead-lag mode in control system designs (Ref. 6).

These studies suggest that considering the rotor's DoF, and in particular lead-lag modes, can be necessary to implement reliable augmented control systems. For this reason, a model complexity analysis is performed in this paper.

The paper is structured as follows. First, a non-parametric system identification is implemented. Then, a parametric transfer function identification is considered to gain information on the dynamics captured in the collected data and to define an adequate state-space model formulation. Finally, a parametric state-space model is identified. A new procedure is proposed to limit the sensitivity to initial parametric values and bounds that affect the minimization of the state-space cost function. The model obtained with this procedure is validated in the time domain to verify its predictive capabilities. Furthermore, a final assessment is made with a helicopter pilot while performing piloted closed-loop control tasks in a CyberMotion Simulator. Conclusions are drawn at the end of the paper.

Frequency domain identification method

The frequency domain system identification method developed by Tischler (Ref. 19) is implemented in this paper using the numerical computation environment MATLAB®. A flowchart showing the main steps of this method is presented in Fig. 1. Advantages of this method include the possibility of implementing non-parametric as well as parametric identification models. Furthermore, bias effects and noise in response measurements can be eliminated. Finally, tools like coherence functions, composite windowing and frequency response conditioning can be used to increase the reliability of the identified model.

In the following sections a brief overview is given of the theory on which the considered identification method is based. Furthermore, results are presented, obtained from applying the identification method on the collected data.

Non-parametric identification

The first step of the system identification method adopted here consists of computing the entire set of nonparametric single-input single-output frequency responses. Generally, for each input-output pair two or three time histories are selected from the collected data and concatenated such that a richer spectral content is obtained within the frequency range of interest. The input-output cross-spectrum $\hat{G}_{xy}(f)$ and the input autospectrum $\hat{G}_{xx}(f)$ estimates are then used to compute the entire set of Single-Input Single-Output (SISO) frequency response estimates:

$$\hat{H}(f) = \frac{\hat{G}_{xy}(f)}{\hat{G}_{xx}(f)} \tag{1}$$

A measure of the quality of a frequency response estimate is the coherence function (Ref. 20), computed as follows:

$$\hat{\gamma}^2_{xy}(f) = \frac{|\hat{G}_{xy}(f)|^2}{|\hat{G}_{xx}(f)||\hat{G}_{yy}(f)|} \tag{2}$$

Coherence function values vary between 0 and 1. A coherence function decrease can be associated with noise, nonlinearities, lack of input excitation or lack of rotorcraft response. In general, coherence values of 0.6 or above are considered satisfactory for system identification purposes (Ref. 21).

An important aspect to take into account is that estimated frequency responses obtained from helicopter

flight data are generally influenced by partially correlated inputs and input-output couplings. These effects can be removed by conditioning the frequency responses and the associated coherence functions. To do so, the conditioned Multi-Input Single-Output (MISO) frequency responses (Ref. 20) are computed for each output as:

$$\hat{\mathbf{H}}(f) = \hat{\mathbf{G}}_{xx}^{-1}(f)\hat{\mathbf{G}}_{xy}(f) \tag{3}$$

where $\hat{\mathbf{G}}_{xy}$ is the vector of SISO cross-spectra between each input and a selected output, and $\hat{\mathbf{G}}_{xx}$ is the matrix containing the inputs auto- and cross-spectra.

The Multi-Input Multi-Output (MIMO) frequency response matrix can be obtained by computing equation 3 for each output and by selecting the frequency responses associated to the primary inputs. This selection is generally done to ensure high coherence in each input-output pair. The partial coherence function associated with each conditioned response is computed as:

$$\hat{\gamma}^2_{x_i y\cdot(n_c-1)!}(f) = \frac{|\hat{G}_{x_i y\cdot(n_c-1)!}(f)|^2}{|\hat{G}_{x_i x_i\cdot(n_c-1)!}(f)||\hat{G}_{yy\cdot(n_c-1)!}(f)|} \tag{4}$$

where n_c is the number of piloted control inputs and $\hat{G}_{x_i y\cdot(n_c-1)!}$ indicates the cross-spectrum estimate between the control input x_i and the output y, conditioned by the other $n_c - 1$ control inputs. Coherently, $\hat{G}_{x_i x_i\cdot(n_c-1)!}$ and $\hat{G}_{yy\cdot(n_c-1)!}$ respectively represent the input and output auto-spectrum estimates conditioned by the other control inputs.

The computation of the MIMO frequency response matrix and of the partial coherence functions represents the last step of the non-parametric model identification.

Transfer function and state-space modeling

The non-parametric model described in the last section represents a starting point for identifying two possible kinds of parametric models: the transfer function and the state-space models. Transfer function models provide useful insight into the order of the system, the level of input-output couplings and fundamental dynamic characteristics of the identified system. Furthermore, initial values of the state-space model parameters can be determined.

State-space models, on the other hand, are better suited for applications that require coupled MIMO behaviors to be captured (e.g. model validation in simulation, high frequency control system design) as

they allow for a simultaneous fitting of the different SISO responses while ensuring coupling constraints.

In the method adopted in this paper, transfer functions models are estimated by fitting the individual conditioned frequency responses computed during the non-parametric identification. The fitting is obtained by minimizing the following cost function (Ref. 19):

$$J_{SISO} = \frac{20}{n_\omega} \sum_{\omega_1}^{\omega_{n_\omega}} W_\gamma \left[W_g \left(\left| \hat{T}_c \right| - |T| \right)^2 + W_p \left(\angle \hat{T}_c - \angle T \right)^2 \right] \tag{5}$$

where $\hat{T}_c$ is the conditioned frequency response estimate obtained from the collected data and T is the selected transfer function model. The frequency points are generally spaced uniformly over a log-frequency scale. A sufficient number of frequency points n_ω is usually considered to be 20 (Ref. 19). In this way the gain in Eq. 5 reduces to 1. Using a larger number of points decreases the cost function value, while a smaller number of points increases it. The frequency range of interest can be freely selected between ω_1 and ω_{n_ω}. An important aspect of this cost function is that response magnitudes and phases are considered separately and scaled with different gains (W_g and W_p) as described in Ref. 19. The choice of W_g and W_p depends on the units used for magnitude and phase, respectively. In this paper, the values listed by USAF MIL-STD-1797B were used: $W_g = 1.0$, $W_p = 0.01745$. The weighting function W_γ depends on the value of the coherence function at each frequency point. Generally, identified transfer function models with associated cost function values $J \leq 100$ have good levels of accuracy and can be used in many key applications, such as handling qualities analysis and control system designs (Ref. 11).

The final step of the identification method adopted here is the realization of a state-space model. The state-space model is defined by truncating at the first order the Taylor series obtained from the general equations of the helicopter dynamics. Furthermore, rotor dynamic equations can be added to account for high frequency modal effects. The result is a hybrid formulation in which stability and control derivatives are the unknowns that need to be estimated (Ref. 13). In the state-space model identification, the minimization is performed by summing the n_{tf} input-output cost functions as defined for the SISO case, see Eq. 5:

$$J_{MIMO} = \sum_{l=1}^{n_{tf}} J_{SISO,l} \tag{6}$$

Generally, each cost function minimization is considered adequate when $J_{SISO,l} \leq 200$. The minimization of the state-space model is considered successful when $J_{MIMO}/n_{tf} \leq 100$. The predictive capability of

the estimated state-space model is usually assessed with a time domain cross-validation by considering flight test data independent from those used during the identification phase (Ref. 19).

The following section presents a brief description of the data collection performed during the flight tests. Then, results are shown, which were obtained by applying the identification theory described above.

Data collection and data analysis

The data used for the identification were collected during two flight tests of one hour each with a Robinson R44 Raven II helicopter. The Robinson R44 is a light weight helicopter with a single engine, a semi-rigid two-bladed main rotor and a two-bladed tail rotor (Ref. 22). The measurement setup used in the two flight tests consisted of two Global Positioning System antennas and an Inertial Measurement Unit composed of Fiber Optic Gyros and Micro Electrical Mechanical System accelerometers. These instruments were used to collect the helicopter response signals: inertial helicopter position (x, y, z), attitude (ϕ, θ, ψ), angular rates (p, q, r) and linear accelerations (a_x, a_y, a_z). These signals were selected as the outputs of the model to identify.

Four optical sensors were placed on the pilot controls to measure the helicopter inputs: longitudinal cyclic stick deflection (δ_{long}), lateral cyclic stick deflection (δ_{lat}), collective lever deflection (δ_{col}) and pedals deflection (δ_{ped}). Measurements of the control displacements should be performed without affecting the test pilot during the flight test. The optical sensors were employed because of their capability of measuring a distance from a specific reference with no mechanical contact. Furthermore, all optical sensors were attached to the controls on the left side of the helicopter, having the pilot sitting on the right-side seat.

Optical sensors can measure linear distances from a specific reference. In the considered measurement setup, the sensors were rigidly attached to the controls, while flat surfaces used as references were located at specific distances. In this way, a continuous measurement was obtained of the distance between the point on the pilot control, on which the sensor was attached, and the surface used as reference. However, helicopter control deflections are better expressed as angles, given the type of motion that they allow. Therefore, a mapping was defined between the measured linear distances and the relative angular deflec-

tions. A detailed description of this mapping can be found in Ref. 23 and is here omitted for the sake of brevity. A schematic representation of the entire setup is given in Fig. 2. All signals were sampled with a frequency rate of 100 Hz.

During the flight tests, several piloted frequency sweeps, doublets and step maneuvers were performed for each control axis (Ref. 19). Doublets and step maneuvers were selected to perform a cross-validation of the identified model in the time domain. The frequency sweeps were chosen for the identification phase. The sweeps were designed with a range of excitation between 0.05 and 2.5 Hz ($\approx$ 0.3 - 16 rad/s) to ensure that important rotor-body coupling dynamics would be excited. An example of frequency sweeps performed in the longitudinal axis is shown in Fig. 3, in which two frequency sweeps of approximately 100 seconds are concatenated. The concatenation is possible because each sweep maneuver starts in the hover flight regime with a few seconds of trim and ends in the same initial trim condition. The longest period contained within the frequency sweep is approximately 20 s (0.05 Hz). Throughout the sweep, the pilot slowly increases the frequency until a period of approximately 0.4 s (2.5 Hz) is achieved. Then the pilot stabilizes the helicopter to the initial trim condition. It can be noticed from the primary axis responses (pitch rate q, pitch angle θ and forward velocity u) that the maneuver was performed correctly as it exhibits low-, medium- and high-frequency components.

After the collection of data, a kinematic data consistency check was performed. The angular consistency was verified by analyzing the frequency responses p/ϕ, q/θ and r/ψ as explained in Ref. 19. This was possible because the maneuvers were restricted to the range of linear kinematics and the wind was calm during the entire flight tests. For the translational consistency check, the reconstructed velocity responses were computed and compared with the responses obtained from the GPS data. A perfect agreement was found between the two responses, which means that the embedded GPS/INS provided kinematically consistent signals. Therefore, the collected accelerations and velocities were considered during the entire system identification process.

Non-parametric identification results

The concatenated signals obtained from the time history data were used to create an entire set of nonparametric single-input single-output frequency responses. An example is presented in Fig. 4a with the Bode plot of the pitch rate response to the longitudinal stick deflection conditioned by the other inputs ($q/\delta_{long} \cdot \delta_{lat}, \delta_{col}, \delta_{ped}$). The figure shows a comparison between three responses obtained with different window lengths and a 50 percent window overlap. Using overlapping windows reduces the random error effects in the spectral estimates (Ref. 19). It can be noticed that the 40 seconds window reduces the random error effects at low frequencies where the coherence reaches high values. However, in the mid- and high-frequency range the response starts to oscillate. In the mid-frequency range the 25 seconds window provides the best result but the response shows again high oscillations at higher frequencies. The 8 seconds window gives poor results at low frequencies (low partial coherence function value) but filters the random error effects at mid- and high- frequencies. Similar results were found in the other input-output pairs. Generally, it is quite challenging to select a window able to provide optimal results over the entire frequency range of interest (Ref. 19). The composite windowing technique described in Ref. 19 solves this issue by merging the responses obtained with different windows into one response estimate with high accuracy over the entire frequency range of interest.

In this paper, the composite windowing technique was applied by selecting five different window lengths. A window of 40 seconds and one of 8 seconds were selected as the largest and the smallest one, respectively. Three more windows were evenly distributed between these two. The resulting composite responses presented a good level of coherence (above the guideline limit of 0.6) over the entire frequency range of interest (0.3 - 16 rad/sec), as shown in Fig. 4b for the pitch-rate response q/δ_{lon}.

The results of the composite windowing showed some important dynamic characteristics captured in the collected data. For the pitch-rate response q/δ_{long} in Fig. 4b the peak at around 1.5 rad/sec can be associated with the short period, while the resonance at 14 rad/sec is due to the lightly damped regressive lead-lag mode.

Another interesting response, shown in Fig. 5, is the vertical acceleration due to the collective deflection, conditioned by the other inputs $a_z/\delta_{col} \cdot \delta_{lat}, \delta_{lon}, \delta_{ped}$. Here, the composite windowing method has

already been applied. As can be seen, the magnitude of the response increases with the frequency. This phenomenon is caused by the inflow effect, a rotor-body coupling mode that appears in hover when the collective position changes rapidly.

Similar rotor-body coupling modes were observed in other on- and off-axis conditioned frequency responses. Therefore, it was concluded that the frequency range of excitation selected during the data collection allowed for rotor-body dynamics to be captured. This result is particularly important as it allows the identification of high order models, which are capable of including rotor/body couplings necessary to implement reliable control designs.

Transfer function modeling results

The selection of the right model structure in the transfer function modeling is crucial to avoid over-parameterizations, which generate poor predictive capabilities. Therefore, the model structure selection is usually done by taking into account the specific application, the frequency range of interest and the physical meaning associated to the selected input-output response. In this work, different models were considered to fit the data response of each input-output axis over the frequency range of interest ($0.3 - 16$ rad/s).

The pitch-rate response q/δ_{lon} and the vertical-acceleration response a_z/δ_{col} will be now considered in detail. These responses are particularly important as they showed rotor-body coupling modes that will be taken into account for selecting the transfer functions orders.

Pitch response

For the identification of the pitch-rate response to the longitudinal stick input q/δ_{lon}, models with order less than 4 were not capable of representing some important dynamic modes, showing cost functions well above the guideline limit of 100. Therefore, a 4th order model and a 6th order model were selected. Both models were able to capture key dynamics associated with the pitch response over the frequency range of interest. The Bode plots of the two models are shown in Fig. 6.

The identified 4th order transfer function model is based on the theory presented in Ref. 24. This model

includes two pairs of poles to identify the low-frequency longitudinal modes of the fuselage dynamics. An equivalent time delay is added to represent the effective delays caused by sensor filtering, linkage dynamics between the stick and the rotor, and additional non-modeled high frequency rotor dynamics. From the minimization of the cost function of Eq. 5, the following transfer function model was obtained:

$$\frac{q}{\delta_{lon}} = \frac{0.14(1.317)[-1, 0.361]e^{-0.023s}}{[-1, 0.733][0.947, 1.33]} \tag{7}$$

where the shorthand notation [ξ,ω] indicates a pair of complex conjugate roots s^2+2$\xi\omega s$+ω^2 with damping ratio ξ and natural frequency ω expressed in rad/sec, while (1/T) indicates a single root s+(1/T). The first pair of poles at 0.733 rad/sec models the unstable longitudinal phugoid mode. It can be noticed that the identified damping ratio of this pair is equal to -1. Therefore, the two poles are unstable and real. The second pair at 1.33 rad/sec is associated with the fuselage short period mode. The effect of this mode in the Bode plot is a decrease both in magnitude and phase, as can be seen in Fig. 6. Finally, an equivalent time delay of 0.023 seconds is identified, which accounts for residual high frequency rotor dynamics. The value of the associated cost function is $J = 37.94$, well within the guideline boundary of 100. This result is reflected in Fig. 6, where it is possible to notice how the 4th order model presents a good level of accuracy over the entire frequency range of interest. However, the model is unable to adequately capture the high frequency lead-lag mode recognized during the nonparametric identification at around 14 rad/sec.

An important measure usually considered to evaluate the fidelity of the identified model with respect to the flight response is the error-response function defined as:

$$\varepsilon_{model}(f) = \frac{T(f)}{\hat{T}_c(f)} \tag{8}$$

with T and $\hat{T}_c$ defined as in Eq. 5.

Magnitude and phase of the error-response function associated to the identified 4th order model are shown in Fig. 7. The mismatch boundaries defined in the USAF MIL-STD-1797B are also shown and represent the Maximum Unnoticeable Added Dynamics (MUAD) limits, useful for handling qualities studies (Ref. 19). As long as these boundaries are not exceeded, an experienced helicopter pilot would hardly detect a divergence in the modeled response characteristics (Ref. 25). Fig. 7 confirms the model incapability to capture the lead-lag mode at 14 rad/sec. Nevertheless, the error value remains within the MUAD mismatch boundaries. Therefore, it can be concluded that the considered 4th order transfer

function model is well suited for handling-qualities analyses, but would not be appropriate for control system designs, in which high frequency rotor dynamics are crucial.

A better result was obtained with the 6th order model, able to capture the regressive lead-lag mode effects as can be seen from the Bode plot in Fig. 6. From the minimization of the cost function of Eq. 5, the following transfer function model was obtained:

$$\frac{q}{\delta_{lon}} = \frac{0.11(3.928)[-1, 0.327][0.213, 14.265]e^{-0.019s}}{[-1, 0.683][0.93, 2.065][0.1, 14.336]} \tag{9}$$

with an associated cost function value $J = 6.17$. In this 6th order model, the phugoid mode is represented with a pair of real unstable poles located at 0.683 rad/sec. The second pair of highly damped complex poles at 2.065 rad/sec models the short period. The rotor lead-lag mode is modeled with a dipole (a pair of conjugate poles at 14.336 rad/sec and a pair of conjugate zeros at 14.265 rad/sec). Finally, a time delay of 0.019 seconds models the residual high frequency rotor dynamics. The error function in Fig. 7 remains within the boundaries over the entire frequency range of interest, which means that a pilot would consider the model responses almost indistinguishable from the actual flight response. It can be concluded that this model is well suited for both handling qualities evaluation and augmented control system design, due to its ability to capture rotor DoFs relevant for this purpose.

Heave response

The transfer function identification of the vertical response is presented here to investigate the inflow dynamic effects shown during the non-parametric identification phase.

Modeling this phenomenon is particularly important to create simulation models in hover that can reproduce the vertical acceleration cues due to rapid collective changes (Ref. 11). Two transfer function models were considered to fit the vertical-acceleration response due to the collective input a_z/δ_{col}. The first one implements the vertical velocity to the collective as a first order function (Ref. 11). The vertical acceleration response is then obtained by multiplication with the Laplace constant s:

$$\frac{a_z}{\delta_{col}} = \frac{0.6035(0)}{(0.5081)} \tag{10}$$

The associated Bode plot is shown in Fig. 8. The related cost function is $J = 145.8$, above the guideline of

100. This is due to the incapability of the model of reproducing the inflow dynamics at high frequencies. However, it is interesting to notice that the error function in Fig. 9 exceeds the MUAD boundaries only at mid-frequencies.

A second model, also presented in Ref. 11, was considered to represent the inflow dynamics neglected in the first model. The model obtained from the minimization is the following:

$$\frac{a_z}{\delta_{col}} = \frac{0.0476(0)(10.3384)e^{-0.0284s}}{(0.2364)} \tag{11}$$

with an associated cost function $J = 15.98$. The Bode plot is shown in Fig. 8. Note that the fitting is improved with respect to the first model because the inflow dynamics are now modeled explicitly. The improvement is also reflected in Fig. 9, where a decrease of the error-response function can be seen at mid- and high-frequencies. From these results it can be concluded that the second model is preferable both for handling qualities evaluations and for control design studies since inflow dynamic effects are adequately identified.

The transfer function modeling was performed for all primary control axes and similar results were obtained as those shown here for the pitch and the heave responses. These responses are not shown here for the sake of brevity. However, the interested reader can find them in Ref. [26]. The information gained from the transfer function identification phase represented a starting point for the implementation of the final state-space model considered in the next sections.

Extended state-space identification

The state-space identification model is generally obtained from the helicopter dynamic equations expanded in a Taylor series and truncated at the first order. The unknown coefficients to be identified are the stability and control derivatives that result from the Taylor series representation. The model structure used for the state space identification is the following:

$$M\dot{\mathbf{x}} = F\mathbf{x} + G\mathbf{u} \tag{12}$$

$$\mathbf{y} = H_0\mathbf{x} + H_1\dot{\mathbf{x}} \tag{13}$$

In this paper, the inputs of the state space model are the four pilot controls

$$\mathbf{u} = [\delta_{lat}, \delta_{lon}, \delta_{ped}, \delta_{col}] \tag{14}$$

the outputs are the helicopter response signals measured during the data collection

$$\mathbf{y} = [u, v, w, p, q, r, a_x, a_y, a_z, \phi, \theta] \tag{15}$$

and the state vector is composed of 20 states that represent the rotor-body dynamics.

$$\begin{aligned}\mathbf{x} = [&u, v, w, p, q, r, \phi, \theta, \beta_{1c}, \beta_{1s}, x_1, x_2, \eta_q, \\ &y_1, y_2, \eta_p, \upsilon, \beta_0, \dot{\beta}_0, \eta_{C_t}]\end{aligned} \tag{16}$$

The M matrix includes parameters that depend on the derivative of the state variables, the F matrix includes the stability derivatives and the G matrix includes the control derivatives. Finally, the two matrices H_0 and H_1 allow the outputs to be expressed in terms of state variables and of their derivatives.

As seen during the transfer function modeling, rotor-body coupling modes (flap, lead-lag and inflow) were captured in the collected data. To include these modes into the state-space model, a hybrid fully coupled formulation was considered. The equations of this formulation will now be described briefly. The meaning of all symbols used in the equations can be found in the Nomenclature.

The rotor/flap body coupling was modeled by adding two coupled first order equations as presented in Ref. 19. The two equations are reported below:

$$\tau_{f_1}\dot{\beta}_{1s} = -\beta_{1s} + Lf_{\beta_{1c}}\beta_{1c} + \tau_{f_1}p + Lf_{\delta_{lon}}\delta_{lon} + Lf_{\delta_{lat}}\delta_{lat} \tag{17}$$

$$\tau_{f_2}\dot{\beta}_{1c} = -\beta_{1c} + Mf_{\beta_{1s}}\beta_{1s} + \tau_{f_2}q + Mf_{\delta_{lon}}\delta_{lon} + Mf_{\delta_{lat}}\delta_{lat} \tag{18}$$

where τ_{f_1} and τ_{f_2} are the lateral and the longitudinal flapping time constants, respectively, while β_{1c} and β_{1s} are the states associated with the longitudinal and the lateral flap dynamics, respectively.

Equations (17,18) are coupled to the roll and the pitch acceleration responses:

$$\begin{aligned}\dot{p} =&L_u u + L_v v + L_w w + L_r r + L_{\beta_{1s}}\beta_{1s}+ \\ &+ L_{\delta_{ped}}\delta_{ped} + L_{\delta_{col}}\delta_{col}\end{aligned} \tag{19}$$

$$\begin{aligned}\dot{q} =&M_u u + M_v v + M_w w + M_r r + M_{\beta_{1c}}\beta_{1c}+ \\ &+ M_{\delta_{ped}}\delta_{ped} + M_{\delta_{col}}\delta_{col}\end{aligned} \tag{20}$$

Here, the effects of the state-space control derivatives ($L_{\delta_{lon}}$, $M_{\delta_{lon}}$, $L_{\delta_{lat}}$, $M_{\delta_{lat}}$) and the effects of the state-space stability derivatives (L_q, M_q, L_p, M_p) are included in the flapping derivatives ($L_{\beta_{1s}}$, $M_{\beta_{1c}}$).

Furthermore, Eqs. (17,18) are coupled to the longitudinal and the lateral linear acceleration equations by adding the state derivatives $X_{\beta_{1c}}$ and $Y_{\beta_{1s}}$:

$$\begin{aligned}\dot{u} = &- W_0 q + V_0 r - (g \cdot cos\Theta_0)\theta + X_u u + X_v v + X_w w + X_r r + \\ &+ X_{\beta_{1c}}\beta_{1c} + X_{\delta_{ped}}\delta_{ped} + X_{\delta_{col}}\delta_{col}\end{aligned} \tag{21}$$

$$\begin{aligned}\dot{v} = &- U_0 r + W_0 p + (g \cdot cos\Theta_0)\phi + Y_u u + Y_v v + Y_w w + Y_p p + Y_r r + \\ &+ Y_{\beta_{1s}}\beta_{1s} + Y_{\delta_{ped}}\delta_{ped} + Y_{\delta_{col}}\delta_{col}\end{aligned} \tag{22}$$

Including the lead-lag dynamics is generally more difficult as no physical models are available in literature. Usually, the lead-lag is implemented as a second order dipole appended to the angular rate responses (Ref. 3, 13). In this way the pitch-rate response with respect to longitudinal stick deflection becomes:

$$\left(\frac{q}{\delta_{lon}}\right)_{lead-lag} = \left(\frac{q}{\delta_{lon}}\right) \cdot \frac{K_p(s^2 + 2\xi_q\omega_q s + {\omega_q}^2)}{s^2 + 2\xi_{ll_r}\omega_{ll_r} s + \omega_{ll_r}^2} \tag{23}$$

The same definition holds for the roll-rate response. The initial values of the dipole parameters are usually fixed to the values identified in the transfer function modeling.

In this paper, the dipole form was directly converted into a canonical form and included in the state-space equations as described in Ref. 27. The canonical form for the pitch axis was implemented as follows:

$$\begin{bmatrix} 1 & 0 & 0 \\ 0 & 1 & 0 \\ 0 & -1 & 1 \end{bmatrix} \cdot \begin{bmatrix} (\dot{x_1})_q \\ (\dot{x_2})_q \\ (\dot{\eta})_q \end{bmatrix} = \begin{bmatrix} 0 & 1 & 0 \\ -{\omega_{ll_r}}^2 & -2\xi_{ll_r}\omega_{ll_r} & 0 \\ {\omega_q}^2 & 2\xi_q\omega_q & 0 \end{bmatrix} \cdot \begin{bmatrix} (x_1)_q \\ (x_2)_q \\ (\eta)_q \end{bmatrix} + \begin{bmatrix} 0 \\ K_q \\ 0 \end{bmatrix} [q] \tag{24}$$

with $\dot{\eta}_q = q_{lead-lag}$. By considering the same state-space canonical form in the roll axis, 6 state variables were introduced: x_1, x_2, η_q for the longitudinal axis and y_1, y_2, η_p for the lateral axis.

Another important dynamic mode captured in the collected data is the coupled fuselage/coning-inflow mode. These dynamics were implemented through the analytical model proposed by Chen and Hindson (Ref. 5). In this model the coning/inflow dynamic equations provide three more states: the inflow ν, the coning angle β_0 and the coning rate $\dot{\beta}_0$.

The inflow is modeled as:

$$\begin{aligned}\dot{\nu} =& \frac{-75\pi\Omega}{32}\left(\bar{\nu}_0 + \frac{a\sigma}{16}\right) C_0\nu + \nu_{\dot{\beta}}\dot{\beta}_0 + \\ &+ \frac{25\pi\Omega^2 R}{32}\left(\frac{a\sigma}{8}\right) C_0 K_{\theta_0}\delta_{col}\end{aligned} \tag{25}$$

The coning dynamics are modeled instead with a second order differential equation:

$$\ddot{\beta}_0 = \frac{-\Omega\gamma}{8}\dot{\beta}_0 - \Omega^2\beta_0 - \frac{\Omega\gamma}{6R}\nu + \frac{\Omega^2\gamma}{8}K_{\theta_0}\delta_{col} \tag{26}$$

The coning/inflow is coupled to the fuselage with a perturbation thrust coefficient introduced as a virtual state derivative $\dot{\eta}_{C_t}$:

$$C_0\dot{\eta}_{C_T} = \frac{0.543}{\Omega^2 R}\dot{\nu} + \frac{4\bar{\nu}_0}{\Omega R}C_0\nu + \frac{4\bar{\nu}_0}{3\Omega}C_0\dot{\beta}_0 \tag{27}$$

Finally, the vertical acceleration equation is expressed as:

$$\begin{aligned}\dot{w} + \left[\frac{\rho\pi R^2(\Omega R)^2}{m}\right]\dot{\eta}_{C_T} =& Z_u u + Z_v v + Z_w w + Z_p p + \\ &+ Z_q q + Z_r r + Z_{\delta_{lon}}\delta_{lon} + \\ &+ Z_{\delta_{lat}}\delta_{lat} + Z_{\delta_{ped}}\delta_{ped}\end{aligned} \tag{28}$$

A final important step is the correction of the collected accelerations when they are not measured at the center of gravity position. In this work the accelerations were measured behind the pilot at the bottom of the rear passenger seat, therefore with a deviation with respect to the center of gravity. To correct for this deviation, longitudinal (x_a) and lateral (y_a) center of gravity positions were computed by using specific software provided by the Robinson helicopter company. However, accurate measurements of the vertical center of gravity position (z_a) are generally very difficult and are not provided by the Robinson software. For this reason, z_a was left as unknown during the identification and included in the model through the equations of longitudinal and lateral accelerations:

$$\begin{aligned}a_x =& \dot{u} + z_a\dot{q} - y_a\dot{r} \\ a_y =& \dot{v} - z_a\dot{p} + x_a\dot{r}\end{aligned} \tag{29}$$

The resulting hybrid state space model implemented through the equations presented in this section contains 12 DoFs that account for rotor/flap body coupling, lead-lag and coning-inflow dynamics. All equation presented here contain many unknown parameters which are to be identified. However, some param-

eters are generally fixed, based on measurements and values provided in literature.

State space modeling results

After selecting the state-space model described in the last section, the procedure presented in Ref. 19 was implemented to identify the unknown parameters. An important feature of this procedure consists of eliminating from the model all parameters considered unidentifiable or that do not possess any physical meaning. This is done based on the insensitivities and the Cramer-Rao bounds associated with the model's parameters. The insensitivity is a measure of the change in the cost function value (Eq. 6) due to a change in a model's parameter. The Cramer-Rao bound is an estimate of the standard deviation associated with an identified parameter. Therefore, it gives an indication of the reliability of the identified value and of its correlation with other parameters. By discarding all parameters considered insignificant or with high correlation, it is possible to obtain a reduced model structure with physical meaning while avoiding over-parameterization.

The unknown parameters of the hybrid model were identified by matching the 44 frequency responses computed in the non-parametric identification. For each response, 20 frequency points were selected in the frequency range of interest (0.3-16 rad/sec) with relative coherence function larger than 0.5, based on the guidelines presented in Ref. 19.

As no direct rotor state measurements were collected, parametric correlation problems were reduced by considering constraints that allow physically meaningful parametric values to be obtained (Ref. 13). The lateral and the longitudinal flapping time delays τ_{f_1} and τ_{f_2} (Eq. 17, 18) were set to be the same ($\tau_f = \tau_{f_1} = \tau_{f_2}$), consistently with the theory predictions (Ref. 19). Furthermore, their values were fixed to the time delay identified during the transfer function modeling of the roll-rate response (p/δ_{lat}). The initial value of the flapping roll spring $L_{\beta_{1s}}$ (Eq. 19) was set to the squared frequency of the roll/flapping mode, obtained from the transfer function identification of the roll-rate response (p/δ_{lat}). Furthermore, the flapping pitch spring $M_{\beta_{1c}}$ initial value (Eq. 20) was set to one-third of the roll spring ($L_{\beta_{1s}}$) value, as predicted by theory. Usually, the coupling terms $Lf_{\beta_{1c}}$, $Lf_{\delta_{lon}}$ (Eq. 17) and $Mf_{\beta_{1s}}$, $Mf_{\delta_{lat}}$ (Eq. 18) are neglected in literature. However, during the identification process a better fitting was achieved by

retaining $Lf_{\beta_{1c}}$, $Lf_{\delta_{lon}}$ in the model. The values of $X_{\beta_{1c}}$ and $Y_{\beta_{1s}}$ in Eqs. 21 and 22 were fixed to g and $-g$, respectively. This choice was based on the assumption that the flapping contribution to longitudinal (X) and lateral (Y) forces is mainly caused by the tilt of the main rotor thrust vector (Ref. 3).

Concerning the lead-lag dynamics (Eq. 23) the denominator terms (damping ratios ξ_{ll_r} and natural frequencies ω_{ll_r}) were constrained to be the same for both the longitudinal and lateral axes, based on symmetry. Moreover, their values were fixed to those obtained from the transfer function identification of the pitch-rate response (Eq. 9). Finally, the time delays were fixed to the values identified during the transfer function modeling.

The state-space identification was possible for 22 of the 44 frequency responses. Table 3 shows for each input/output pair the final range of frequencies included in the cost function calculation. As can be seen, most of the secondary responses in the vertical and in the yaw control axes were discarded due to low coherence (less than 0.6) throughout the entire frequency range of interest. The algorithm used to minimize the MIMO cost function (Eq. 6) was sensitive to initial parametric values and bounds. As a result of this, different local minima were obtained. An iterative pattern search algorithm is generally used to overcome this issue, as proposed by Tischler (Ref. 19). However, this solution did not achieve satisfactory results as poor fits were obtained in many responses (high values of cost-function).

Therefore, a new procedure was proposed composed of two main steps. The first step consists of selecting a larger number of frequency points (50 instead of 20). Furthermore, the points are included if the associated partial coherence function ($\hat{\gamma}^2$) is larger than 0.3, instead of the 0.5 usually adopted in literature. Although the selection of these parameters is not based on theoretical analyses, it is assumed that including additional points with lower coherence increases the frequency content of the data used in the model fitting. The optimization problem is then performed with the new selected parameters. During the optimization, the selected frequency points are weighted with the associated coherence values. By applying this first step, solutions were obtained that are less sensitive to initial parametric values and boundaries.

However, low coherence values are generally associated with process noise, nonlinearities, lack of input excitation or lack of rotorcraft response. For this reason, a second step is included in the procedure in which the original guidelines (20 frequency points and partial coherence $\hat{\gamma}^2 > 0.5$) are again applied to

fit the final state-space model. This time though, local minima are avoided by selecting initial parametric values and boundaries based on the solutions given by the first step of the new procedure.

The identified parameters of the final model obtained by applying this procedure are listed in Table 1 and in Table 2 with the associated Cramer-Rao bounds and insensitivities. As can be noticed, the model is characterized by an acceptable theoretical accuracy since only the speed-damping derivative Y_v has relative Cramer-Rao bound larger than 20% and an insensitivity value larger than 10%, which are usually defined in literature as desired maximum values. For this reason, the Y_v speed-damping derivative was individually identified by fitting the frequency response $\dot{v}/\phi$ with a first order transfer function, as shown in Ref. 19. A value of -0.0089 was identified in this way. However, fixing this value in the model structure resulted in a large marginal increase of the overall cost function (Eq. 6). For this reason, the speed-stability derivative Y_v was eventually left as a free parameter in the identification of the state-space model. Furthermore, during the identification it was verified that dropping this parameter from the model led to a large marginal increase in the overall model cost function. Therefore, the model was not further reduced.

The pitch-rate and the heave responses are now considered in detail and compared to the results obtained in the transfer function identification. Fig. 10 shows the pitch-rate response to the longitudinal stick input (q/δ_{lon}). As expected, a less accurate fitting is achieved at low frequencies with respect to the transfer function identification (Fig. 6) since 22 responses are simultaneously fitted in the state-space identification. Nevertheless, the obtained pitch-rate cost function is $J_{q/\delta_{lon}} = 74.38$, well below the guideline limit of 200. The final model is able to represent the low-frequency phugoid oscillation with a pair of unstable complex poles located at 0.541 rad/sec. This frequency value is very close to the value identified in the transfer function modeling (0.683 rad/sec). As can be noticed in Fig. 10, the model is able to represent the lead-lag mode. The identified parameters associated with this mode are also listed in Table 1. Of these parameters, the terms corresponding to the lead-lag dipole numerator (ξ_{ll_r},ω_{ll_r}) were left to be determined during the identification. Those corresponding to the denominator (ξ_q,ω_q) were fixed to the values identified during the transfer function modeling (Eq. 9).

The vertical-acceleration response to the collective input (a_z/δ_{col}) is shown in Fig. 11. The good quality of the fit in the frequency range of interest ($0.3 - 16$ rad/s) is reflected in the low cost function $J_{a_z/\delta_{col}} = 62.98$. However, it is interesting to notice that despite the inclusion of the coning-inflow dynamics and

the high value of the associated partial coherence function, the model is not able to reproduce the phase increase at high frequencies. This was attributed to the selected representation in state-space form of the coning-inflow dynamics. Indeed, Fig. 8 showed that the coning-inflow representation used for the transfer function modeling was able to reproduce this response behavior. However, to the best of the authors knowledge, limitations concerning the state-space representation of the coning-inflow dynamics are not described in literature. Therefore, reasons for this result should be further investigated.

In the state-space identification the p/δ_{lon} frequency response (Fig. 12) achieved the worst fitting with a cost function of 315. This result was attributed to the particularly high random error of the response at high frequencies. However, the response was not discarded since it showed a high partial coherence function ($\hat{\gamma}^2$) in a sufficient number of points within the frequency range of interest. Furthermore, despite the high associated cost function, the identified state-space model was able to resemble the measured response behavior in the frequency range of interest.

For the frequency responses that are not shown here, the identification provided results that are similar to those presented in this section. This can be seen in the other on-axis responses shown in the Appendix.

Validation of the state-space model

The identified state-space model presented in the last section was validated in the time domain to test its predictive capabilities with respect to different inputs (doublets) than those considered during the identification (frequency sweeps). Figs. 13 and 14 show the difference between the flight test data and the model responses to a doublet given in one of the four control axes.

As can be seen in Fig. 13a, a very good agreement is achieved in the lateral axis between the model and the collected data. However, the model exaggerates the yaw-rate response (r/δ_{lat}) at low frequencies. A satisfactory result is also achieved in the longitudinal axis (Fig. 13b). In particular, it can be noticed that the off-axis roll-rate response (p/δ_{lon}) follows the data well, despite the poor fit in the associated frequency response (Fig. 12). As for the lateral axis, the yaw-rate response (r/δ_{lon}) shows some discrepancies.

The yaw and the vertical axes have excellent agreements in the on-axes responses but the model pre-

dictive capabilities worsen in the off-axes responses (Figs. 14a and 14b). This reflects the result obtained during the identification, in which most of the off-axes responses were discarded because of low frequency content over the entire frequency range of interest. An important limitation of the model is its inability to properly predict the helicopter yaw/heave coupling (r/δ_{col}). This was attributed to a high coupling between collective and pedals inputs given by the pilot during the flight tests, which could also explain the discrepancies in the yaw-rate responses observed in both longitudinal and lateral axes. Despite these limitations, the model shows good predictive capabilities and the ability to capture important characteristics for handling qualities analysis and control system design.

A final model assessment was done by performing hover and low speed closed-loop control task maneuvers with an experienced helicopter pilot in the MPI CyberMotion Simulator (Ref. 28). The pilot's experience consisted of 110 flight hours and more than 500 take-offs and landings. Most of his training was performed with an Alouette II Sud-Est SE.3130 helicopter. Furthermore, he performed 4 hours of training on a motion simulator with a Bell UH-1D model.

The pilot assessed the model in visual-only-condition first and in visual-plus-motion-condition after. The simulator cabin was equipped with a pilot seat, a conventional center-stick cyclic, a collective lever and rudder pedals. A virtual environment representing an airport was projected inside the simulator cabin showing a helicopter pilot perspective. All trials started in hover with all controls at zero position. The pilot had full control of all axes. First, longitudinal and lateral doublets were performed. The pilot appreciated the coupling between the two axes that he described as "quite realistic". The motion in both axes was considered "very good". The vertical and yaw axes were analyzed next. Again some doublets were performed in both axes. The pilot described the pedals as "more sensitive than expected". However, he appreciated the range of motion associated with the yaw axis. The yaw-heave coupling was considered "different than in a real helicopter" in agreement with the validation results. However, he indicated that he was "positively surprised by the model's capability of capturing these helicopter characteristics". Finally, the pilot was instructed to perform maneuvers in hover and the low speed flight regime. The model was overall assessed as "quite good and realistic". The positive feedback given by the helicopter pilot confirmed the results obtained in the time validation.

Conclusions

This paper presented results on the implementation of a fully coupled state-space model of a Robinson R44 helicopter in hover. The frequency responses obtained from the collected data showed that the chosen frequency range of excitation ($0.3 - 16$ rad/s) allows rotor-body coupling modes of the helicopter to be captured. A transfer function identification was first performed to gain important information concerning order of the system, level of input-output couplings and initial values of some state-space parameters. Then, the main dynamic equations necessary to represent rotor-body couplings in state-space form were introduced and the state-space identification was performed. A new procedure was proposed to limit the sensitivity of the state-space minimization algorithm to initial parametric values and bounds. The state-space model obtained with this procedure showed good predictive capabilities, being able to capture high frequency rotor-body coupling dynamics. A further validation of the model was made with an experienced helicopter pilot while performing piloted closed-loop control tasks in the MPI CyberMotion Simulator. The positive feedback given by the pilot confirmed the results obtained in the time validation.

The paper showed that the proposed new procedure and the adopted identification method allow for reliable state-space models to be obtained. The model implemented here was proven to be suitable for handling qualities studies, high frequency control system designs and realistic simulations that involve piloted closed-loop control tasks.

The results of this paper represent a contribution towards the application of system identification studies in the civil helicopter domain. Indeed, the civil helicopter community could significantly benefit from system identification studies that could be used to improve stability and maneuverability of existing helicopters and to achieve higher safety and performance levels.

References

[1]Klein, V. and Morelli, E. A., *Aircraft system identification: Theory and Practice*, AIAA American Institute of Aeronautics and Astronautics Reston, VA, USA, 2006.

[2]Hamel, P. G. and Kaletka, J., "Advances in rotorcraft system identification," *Progress in Aerospace Sciences*, Vol. 33, March-April 1997, pp. 259–284.

[3]Fletcher, J. W., "Identification of UH-60 Stability Derivative Models in Hover from Flight Test Data," *Journal of the American Helicopter Society*, Vol. 40, (1), January 1995, pp. 32–46.

[4]"AGARD Lecture Series 178, Rotorcraft System Identification," Technical report, AGARD Advisory Group for Aerospace Research & Development, 7 Rue Ancelle, 92200 Neuilly Sur Seine, France, 1995.

[5]Chen, R. T. N. and Hindson, W. S., "Influence of Higher-Order Dynamics on Helicopter Flight Control System Band-width," *Journal of Guidance, Control, and Dynamics*, Vol. 9, (2), March-April 1986, pp. 190–197.

[6]Greiser, S. and Lantzsch, R., "Equivalent Modelling and Suppression of Air Resonance for the ACT/FHS in Flight," Proceedings of the 39th European Rotorcraft Forum, Moscow, Russia, September 3-6, 2013.

[7]Tischler, M. B. and Remple, R. K., *Aircraft and Rotorcraft System Identification Engineering Methods with Flight Test Examples*, AIAA Education Series, 2006.

[8]Ivler, C. and Tischler, M., "Case Studies of System Identification Modeling for Flight Control Design," *Journal of the American Helicopter Society*, Vol. 58, (1), January 2013, pp. 1–16.

[9]Jategaonkar, R. V., Fischenberg, D., and Gruenhagen, W., "Aerodynamic Modeling and System Identification from Flight Data-Recent Applications at DLR," *Journal of Aircraft*, Vol. 41, (4), JulyAugust 2004, pp. 681–691.

[10]Baskett, B. J., "Aeronautical Design Standard Performance Specification Handling Qualities Requirements for Military Rotorcraft," Technical Report ADS-33E-PRF, United States Army Aviation and Missile Command, Aviation Engineering Directorate, Redstone Arsenal (AL), 2000.

[11]Ham, J. A., Gardner, C. K., and Tischler, M. B., "Flight Testing and Frequency Domain Analysis for Rotorcraft Handling Qualities," *Journal of the American Helicopter Society*, Vol. 40, (2), April 1995, pp. 28–38.

[12]Dorobantu, A., Murch, A., Mettler, B., and Balas, G., "System Identification for Small, Low-Cost, Fixed-Wing Unmanned Aircraft," *Journal of Aircraft*, Vol. 50, (4), June 2013, pp. 1117–1130.

[13]Tischler, M. B. and Cauffman, M. G., "Frequency Response Method for Rotorcraft System Identification: Flight Applications to BO 105 Coupled Rotor/Fuselage Dynamics," *Journal of the American Helicopter Society*, Vol. 37, (3), July 1992, pp. 3–17.

[14]Fu, K. H. and Kaletka, J., "Frequency-Domain Identification of BO 105 Derivative Models with Rotor Degrees of Freedom," *Journal of the American Helicopter Society*, Vol. 38, (1), January 1993, pp. 73–83.

[15]Kaletka, J., Kurscheid, H., and Butter, U., "FHS, the new research helicopter: Ready for service," *Aerospace science and technology*, Vol. 9, (5), July 2005, pp. 456–467.

[16]Greiser, S. and von Gruenhagen, W., "Analysis of Model Uncertainties Using Inverse Simulation," Proceedings of the 69th Annual Forum of the American Helicopter Society, Phoenix, Arizona, May 21-23, 2013.

[17]Zivan, L. and Tischler, M. B., "Development of a Full Flight Envelope Helicopter Simulation Using System Identification," *Journal of the American Helicopter Society*, Vol. 55, (2), April 2010, pp. 22003.

[18]Tischler, M. B., "System Identification Requirements for High-Bandwidth Rotorcraft Flight Control System Design," *Journal of Guidance, Control, and Dynamics*, Vol. 13, (5), September-October 1990, pp. 835–841.

[19]Tischler, M. B. and Remple, R. K., *Aircraft and Rotorcraft System Identification Engineering Methods with Flight Test Examples*, AIAA Education Series, 2012.

[20]Bendat, J. S. and Piersol, A. G., *Random Data: Analysis and Measurement Procedures, Fourth Edition*, John Wiley & Sons, 2010.

[21]Sahai, R., Cicolani, L., Tischler, M., Blanken, C., Sullivan, C., Wei, M., Ng, Y.-S., and Pierce, L., "Flight-time identification of helicopter-slung load frequency response characteristics using CIFER," Proceedings of the 24th Atmospheric Flight Mechanics Conference, Portland, August 9-11, 1999.

[22]"R44 II Pilot's Operating Handbook," Technical report, Robinson Helicopter Company, 1992.

[23]Geluardi, S., Nieuwenhuizen, F. M., Pollini, L., and Bülthoff, H. H., "Data collection for developing a dynamic model of a light helicopter," Proceedings of the 39th European Rotorcraft Forum, Moscow, Russia, September 3-6, 2013.

[24]Heffley, R. K., "A Compilation and Analysis of Helicopter Handling Quality Data," Technical Report NASA-CR-314, National Aeronautics and Space Administration, Scientific and Technical Information Branch, 1979.

[25]Tischler, M. B., "System Identification Methods for Aircraft Flight Control Development and Valida-

tion," Technical Report NASA-TM-110369, Aeroflightdynamics Directorate, U.S. Army ATCOM, Ames Research Center, Moffett Field, CA 94035-10008, October 1995.

[26]Geluardi, S., Nieuwenhuizen, F. M., Pollini, L., and Bülthoff, H. H., "Frequency Domain System Identification of a Light Helicopter in Hover," Proceedings of the 70th Annual Forum of the American Helicopter Society, Montreal, Canada, May 20-22, 2014.

[27]Quiding, C., Ivler, C. M., and Tischler, M. B., "GenHel S-76C Model Correlation using Flight Test Identified Models," Proceedings of the 64th Annual Forum of the American Helicopter Society, Montreal, Canada, 29 April - 1 May, 2008.

[28]Nieuwenhuizen, F. M. and Bülthoff, H. H., "The MPI CyberMotion Simulator: A Novel Research Platform to Investigate Human Control Behavior," *Journal of Computing Science and Engineering*, Vol. 7, (2), 2013, pp. 122–131.

List of Figures

List of Tables

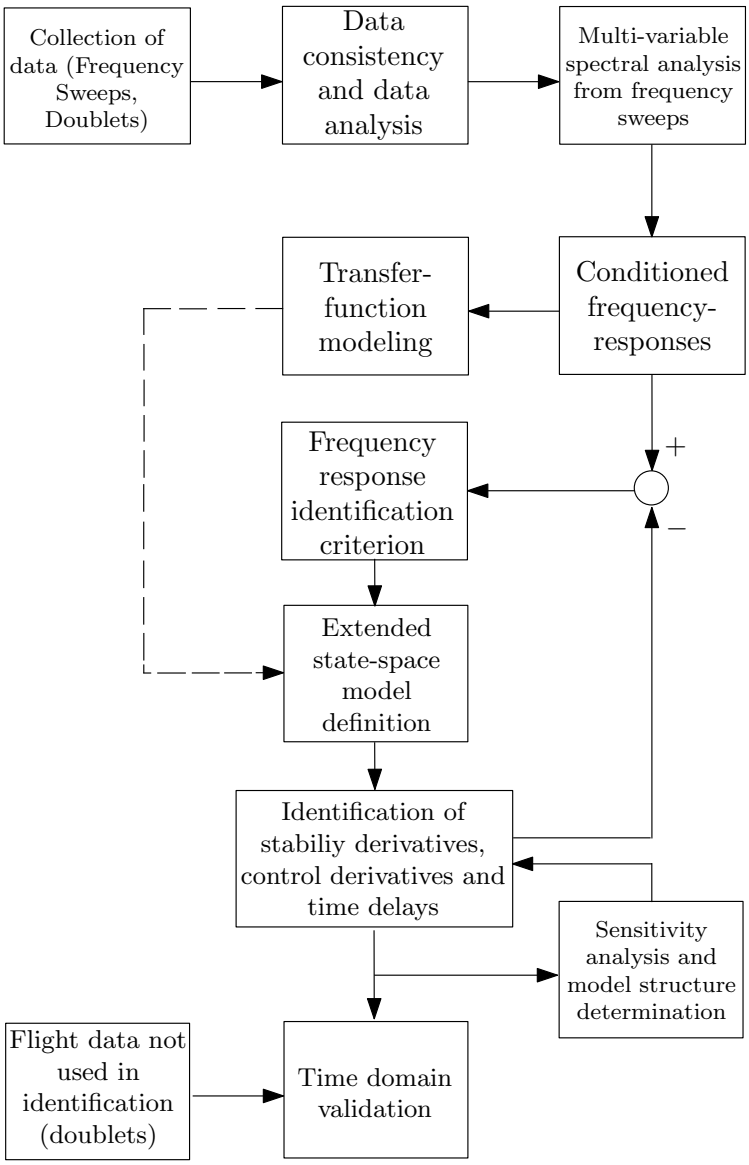

Fig. 1: Flowchart frequency-response system identification method.

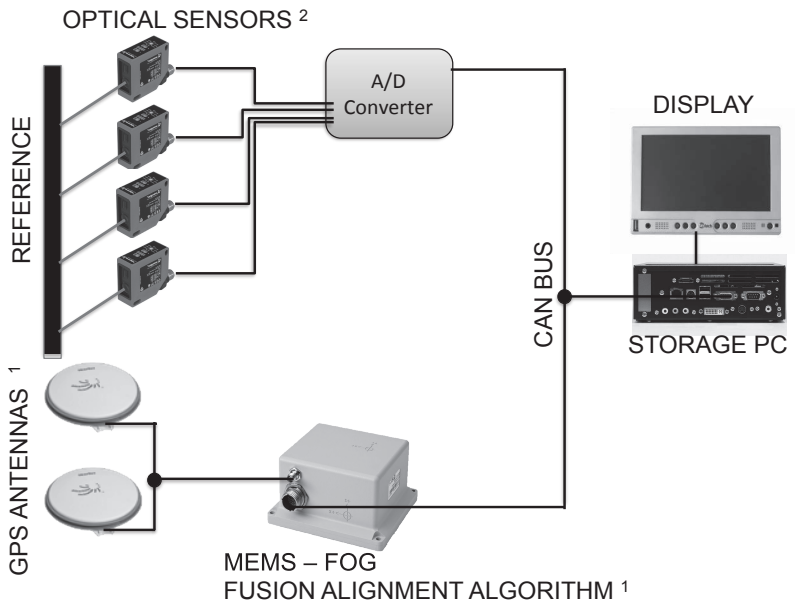

[1]http://www.novatel.com/products/span-gnss-inertial-systems/span-combined-systems/span-cpt

[2]http://www.wenglor.com

Fig. 2: Schematic overview of the measurement setup. Four optical sensors measure the pilot controls displacements with respect to reference plates. Two GPS antennas and an IMU measure the helicopter response.

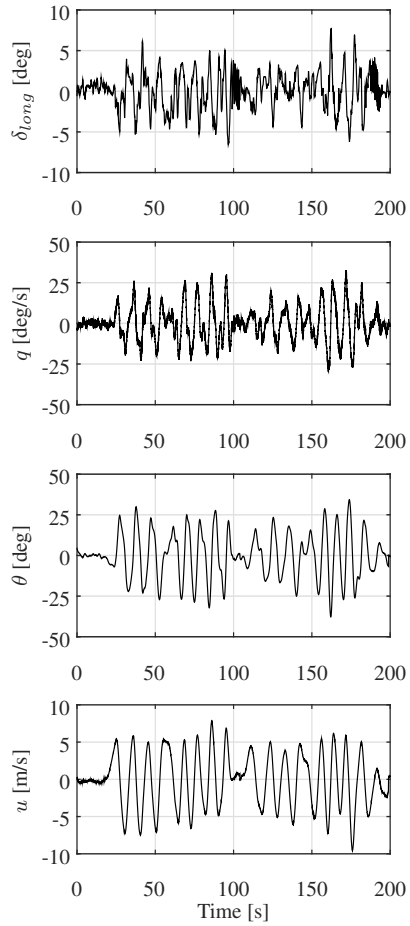

Fig. 3: Frequency sweeps in longitudinal axis, hover condition. δ_{lon} = cyclic longitudinal deflection, u = longitudinal translational velocity, θ = pitch angle, q = pitch rate.

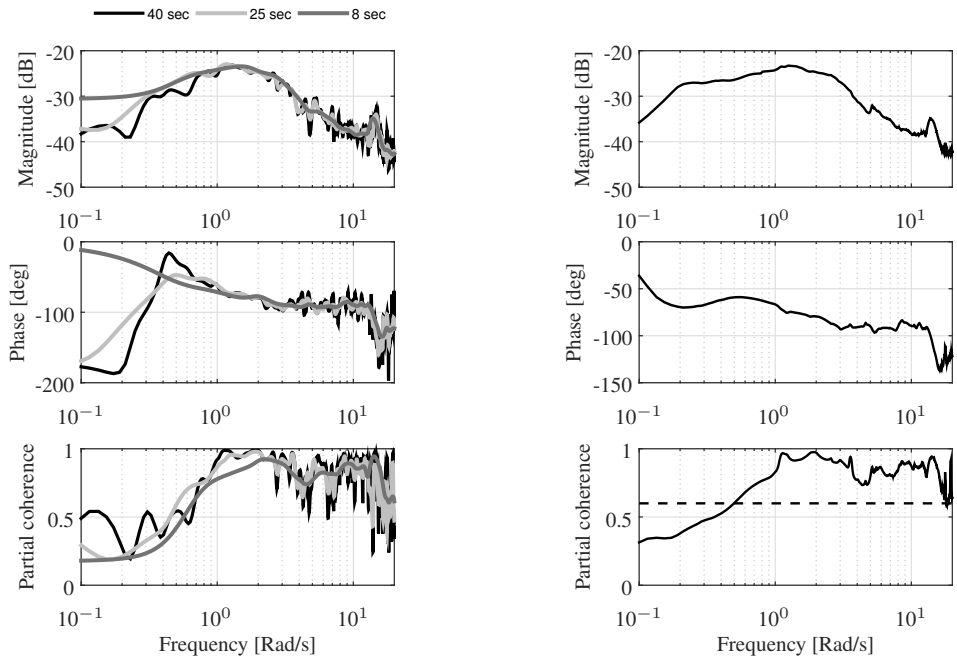

(a) Different windows length

(b) Windowing method applied

Fig. 4: Pitch axis frequency response q/δ_{lon} composite windowing method. The dashed line represents a coherence value of 0.6. Values of coherence above this value are considered good.

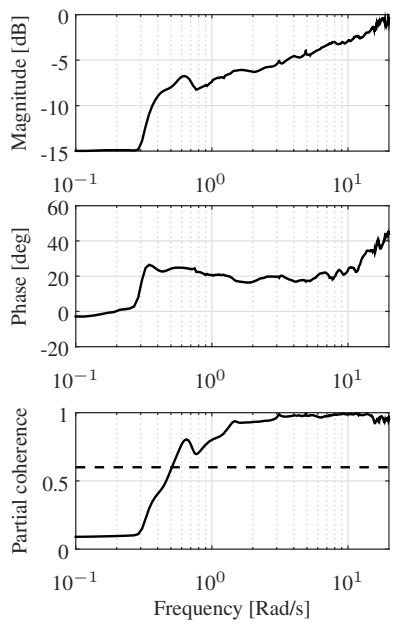

Fig. 5: Vertical MISO conditioned frequency response a_z/δ_{col} with composite windowing method applied. The dashed line represents a coherence value of 0.6. Values of coherence above this value are considered good.

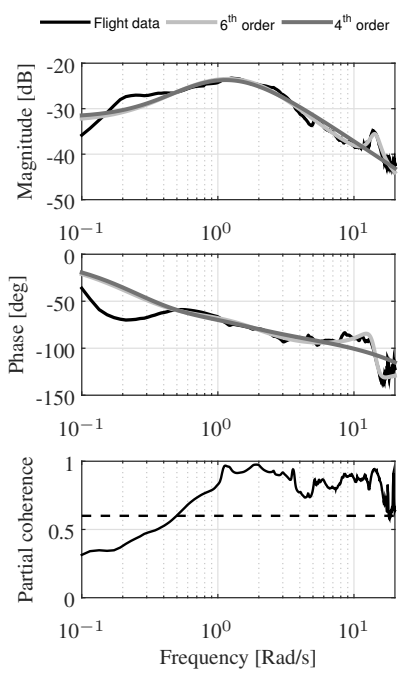

Fig. 6: Bode plot transfer function models for the pitch response q/δ_{lon}. The dashed line represents a coherence value of 0.6. Values of coherence above this value are considered good.

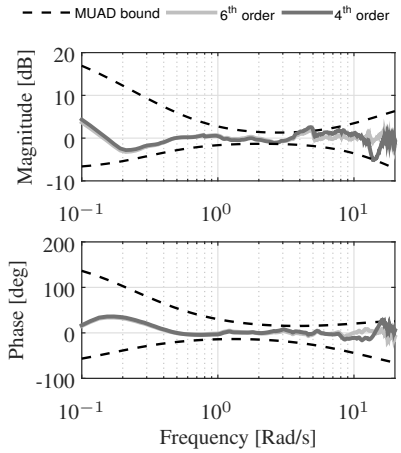

Fig. 7: Error transfer function of the q/δ_{long} response for the 4th and the 6th order model with Maximum Unnoticeable Added Dynamics (MUAD) boundaries.

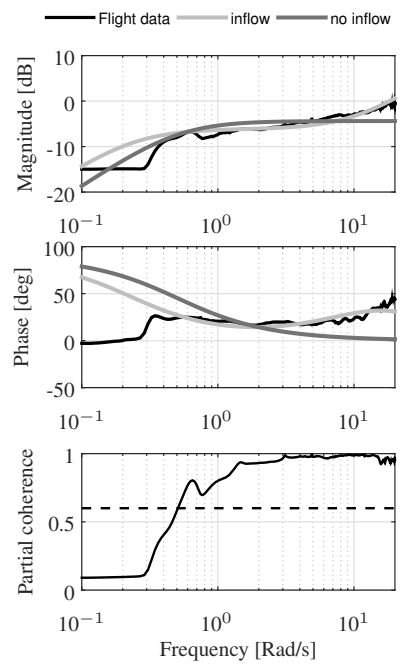

Fig. 8: Bode plot transfer function models for the vertical-acceleration response due to the collective input a_z/δ_{col}. Two models are compared, one capable of capturing the inflow and the other one unable (no inflow). The dashed line represents a coherence value of 0.6. Values of coherence above this value are considered good.

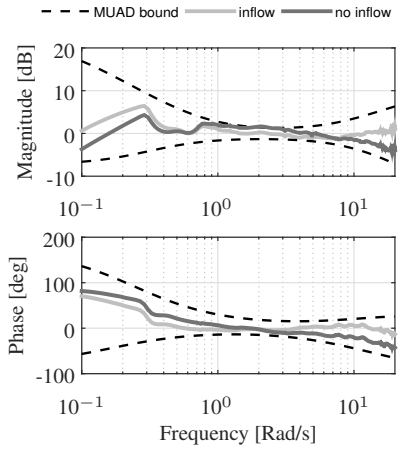

Fig. 9: Error transfer function of the vertical-acceleration response due to the collective input a_z/δ_{col} with Maximum Unnoticeable Added Dynamics (MUAD) boundaries. Two models are compared, one capable of capturing the inflow and the other one unable (no inflow)

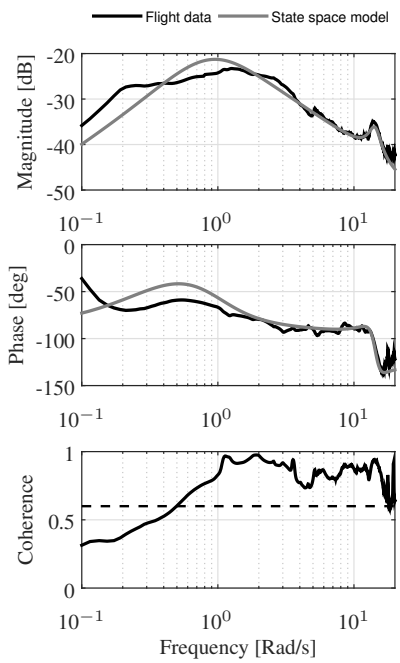

Fig. 10: Bode plot state space model pitch response to longitudinal cyclic q/δ_{lon}.

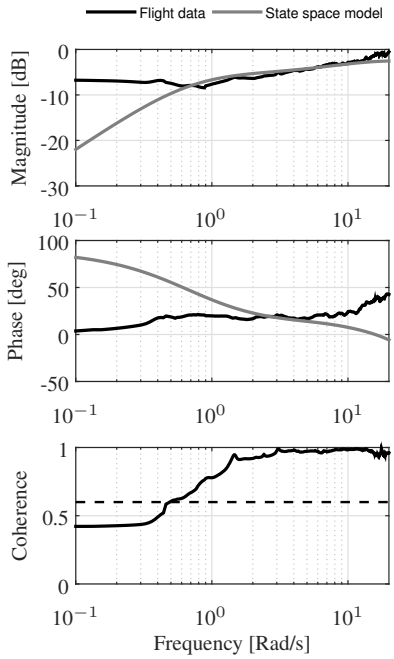

Fig. 11: Bode plot of state space model's vertical response to collective a_z/δ_{col}.

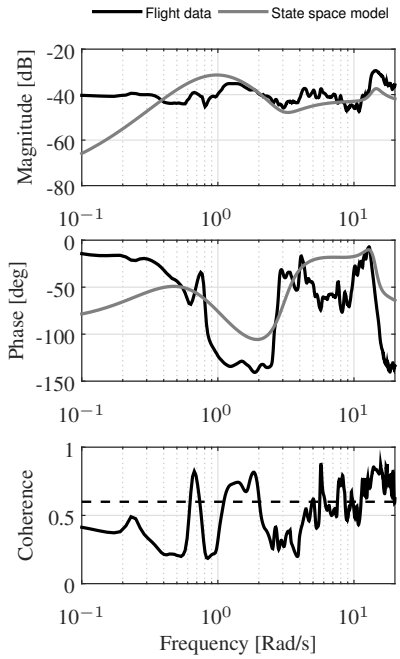

Fig. 12: Bode plot of state space model's roll response to longitudinal cyclic p/δ_{lon}.

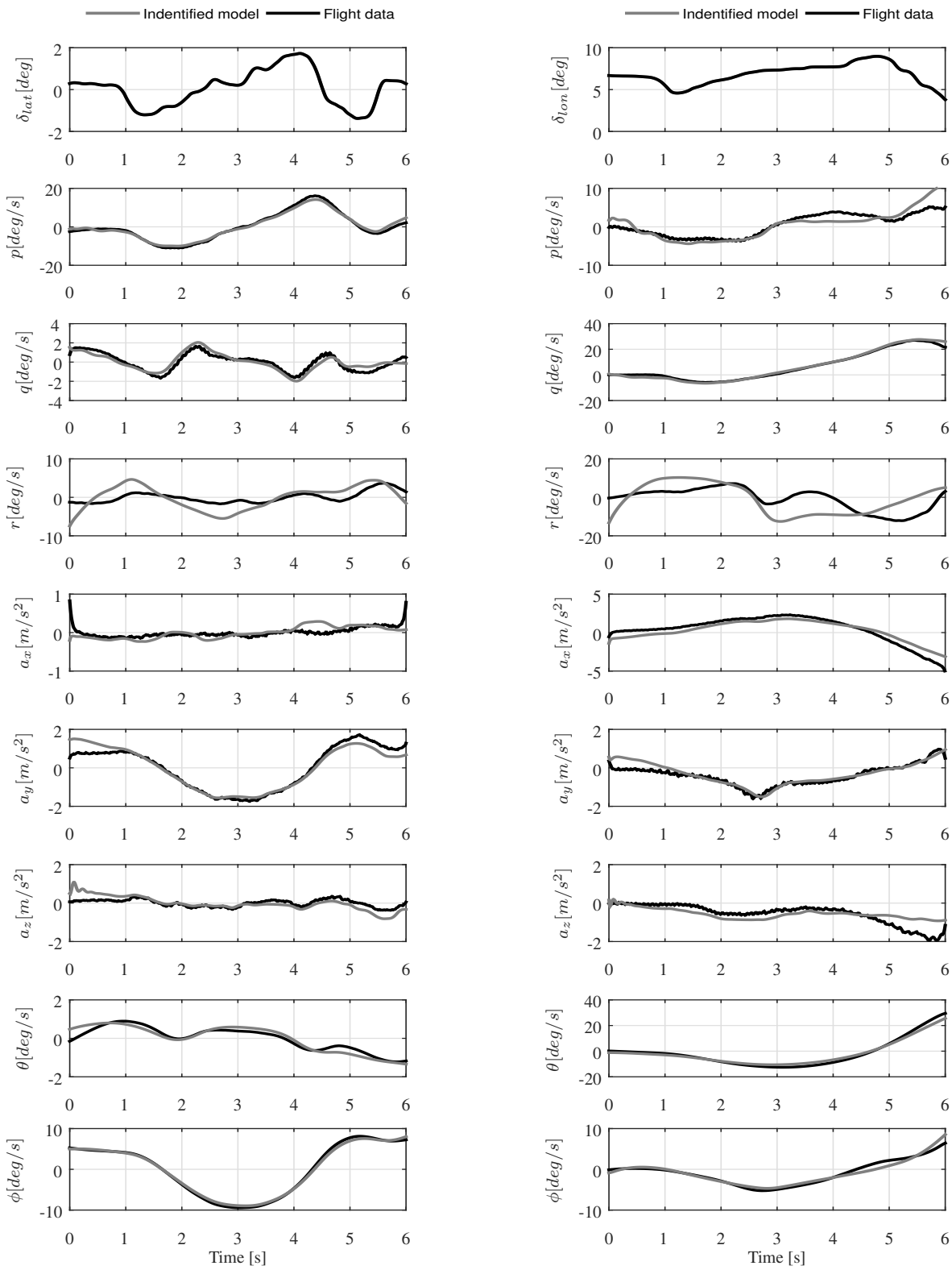

(a) Lateral Cyclic doublet

(b) Longitudinal Cyclic doublet

Fig. 13: Time validation with Lateral Cyclic and Longitudinal Cyclic doublets

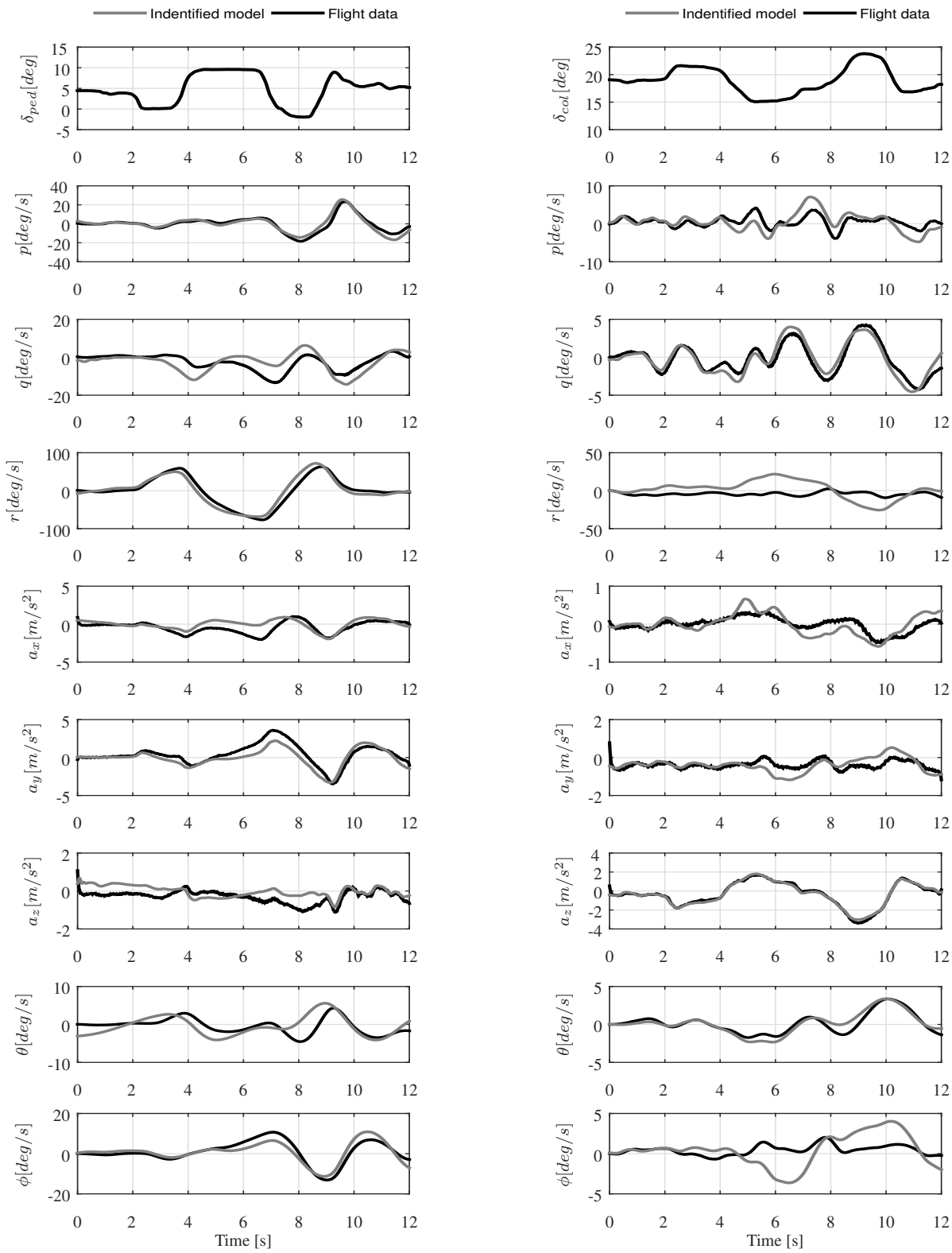

(a) Pedals doublet

(b) Collective doublet

Fig. 14: Time validation with Pedals and Collective doublets

Table 1: Model parameters (M-matrix and F-matrix)

Derivative	Value	C.R. (%)	Insens. (%)
X_u	-0.354	12.757	5.396
X_v	0[1]	n/a	n/a
X_w	0[1]	n/a	n/a
X_p	0[1]	n/a	n/a
X_q	0[1]	n/a	n/a
X_r	0[1]	n/a	n/a
$X_{\beta_{1c}}$	9.810[2]	n/a	n/a
Y_u	0[1]	n/a	n/a
Y_v	-0.144	35.945	16.241
Y_w	0[1]	n/a	n/a
Y_p	0[1]	n/a	n/a
Y_q	0[1]	n/a	n/a
Y_r	0[1]	n/a	n/a
$Y_{\beta_{1s}}$	-9.810[2]	n/a	n/a
Z_u	0[1]	n/a	n/a
Z_v	0[1]	n/a	n/a
Z_w	-0.324	15.328	6.944
Z_p	0.754	16.003	7.318
Z_q	0[1]	n/a	n/a
Z_r	0[1]	n/a	n/a
L_u	0[1]	n/a	n/a
L_v	0.064	12.235	3.461
L_w	0[1]	n/a	n/a
L_r	0[1]	n/a	n/a
$L_{\beta_{1s}}$	44.022	7.090	0.878
M_u	-0.042	9.092	2.836
M_v	0[1]	n/a	n/a
M_w	0[1]	n/a	n/a
M_p	-0.304	8.988	3.472
M_r	0[1]	n/a	n/a
$M_{\beta_{1c}}$	9.053	5.195	0.905
N_u	0[1]	n/a	n/a
N_v	0[1]	n/a	n/a
N_w	-0.254	7.496	3.106
N_p	-0.288	19.960	8.839
N_q	0[1]	n/a	n/a
N_r	-1.193	6.153	2.452
$N_{\beta_{1s}}$	7.106	10.185	2.548
$Lf_{\beta_{1c}}$	-0.745	8.081	0.169
$Mf_{\beta_{1s}}$	0[1]	n/a	n/a
K_p	1.062	7.091	1.649
ω_p^2	187.886	4.749	1.259
$2\xi_p\omega_p$	4.869	12.289	4.891
$\omega_{ll_r}^2$	-205.521[2]	n/a	n/a
$2\xi_{ll_r}\omega_{ll_r}$	-2.867[2]	n/a	n/a
K_q	1.205	9.699	1.965
ω_q^2	215.379	7.370	1.697
$2\xi_q\omega_q$	6.689	16.322	6.383
$\omega_{ll_{r_2}}^2$	-205.521[2]	n/a	n/a
$2\xi_{ll_{r_2}}\omega_{ll_{r_2}}$	-2.867[2]	n/a	n/a
τ_f	-0.026[2]	n/a	n/a
$\nu_{\dot{\beta}}$	-18.962[2]	n/a	n/a
C_0	0.639[2]	n/a	n/a
K_{θ_0}	-0.0055	3.083	1.292
R	5.029[2]	n/a	n/a
a	5.73[2]	n/a	n/a
m	1015[2]	n/a	n/a
γ	3.2727[2]	n/a	n/a
ρ	1.2[2]	n/a	n/a
σ	0.0322[2]	n/a	n/a
$\bar{\nu}_0$	0.0342[2]	n/a	n/a
Ω	42[2]	n/a	n/a

[1] Eliminated during model determination

[2] Fixed value in model

Table 2: Model parameters (G-matrix, H-matrix and time delays)

Derivative	Value	C.R. (%)	Insens. (%)
X_{lat}	0[1]	n/a	n/a
X_{lon}	0[1]	n/a	n/a
X_{ped}	0[1]	n/a	n/a
X_{col}	0[1]	n/a	n/a
Y_{lat}	0[1]	n/a	n/a
Y_{lon}	0[1]	n/a	n/a
Y_{ped}	0[1]	n/a	n/a
Y_{col}	0[1]	n/a	n/a
Z_{lat}	0[1]	n/a	n/a
Z_{lon}	0[1]	n/a	n/a
Z_{ped}	0[1]	n/a	n/a
Z_{col}	0[1]	n/a	n/a
L_{lat}	0[1]	n/a	n/a
L_{lon}	0[1]	n/a	n/a
L_{ped}	0[1]	n/a	n/a
L_{col}	0[1]	n/a	n/a
M_{lat}	0[1]	n/a	n/a
M_{lon}	0[1]	n/a	n/a
M_{ped}	0[1]	n/a	n/a
M_{col}	0[1]	n/a	n/a
N_{lat}	0[1]	n/a	n/a
N_{lon}	0[1]	n/a	n/a
N_{ped}	0.312	2.434	1.089
N_{col}	0[1]	n/a	n/a
$Lf_{\delta_{lon}}$	0.0074	9.913	0.158
$Lf_{\delta_{lat}}$	0.0067	7.139	0.805
$Mf_{\delta_{lon}}$	0.0095	5.556	0.164
$Mf_{\delta_{lat}}$	0[1]	n/a	n/a
z_a	0.143	19.415	5.871
τ_{lat}	0.001[2]	n/a	n/a
τ_{lon}	0.019[2]	n/a	n/a
τ_{ped}	0[2]	n/a	n/a
τ_{col}	0.028[2]	n/a	n/a

[1] Eliminated during model determination

[2] Fixed value in model

Table 3: Frequency-response ranges

Response	Control (input)			
	δ_{lat}	δ_{lon}	δ_{ped}	δ_{col}
u	None	1-2.6 rad/sec	1.2-12.8 rad/sec	None
v	1.2-12 rad/sec	None	1.4-14.5 rad/sec	None
w	None	None	None	0.3-20 rad/sec
p	0.5-16 rad/sec	0.6-16 rad/sec	None	None
q	None	0.3-16 rad/sec	None	None
r	1.4-13 rad/sec	None	1.1-16 rad/sec	0.5-2.8 rad/sec
a_x	1-14 rad/sec	0.9-3.3 rad/sec	1.1-15.5 rad/sec	None
a_y	1.1-15 rad/sec	0.4-3 rad/sec	1.4-15.7 rad/sec	None
a_z	1.8-14 rad/sec	None	None	0.4-20 rad/sec
θ	None	1-15 rad/sec	None	None
ϕ	1.1-14 rad/sec	0.4-1.9 rad/sec	None	None

Appendix

In this appendix the on-axis Bode plots are shown for each control axis. In each plot, the frequency response obtained from the collected flight data is shown in terms of magnitude, phase and coherence. Furthermore, the responses of the identified state-space model are shown.

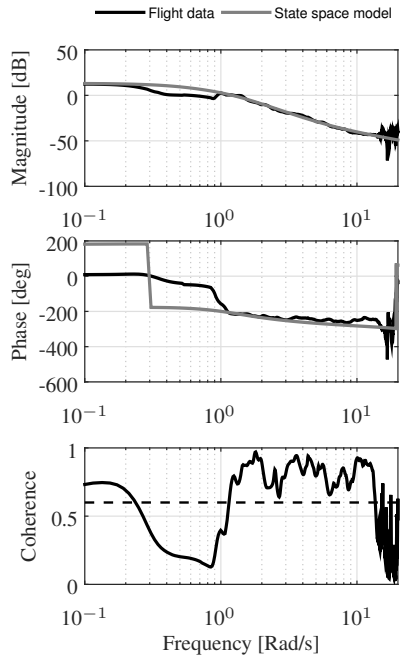

Fig. 15: Bode plot of state space model's lateral translational velocity to lateral cyclic input (v/δ_{lat}).

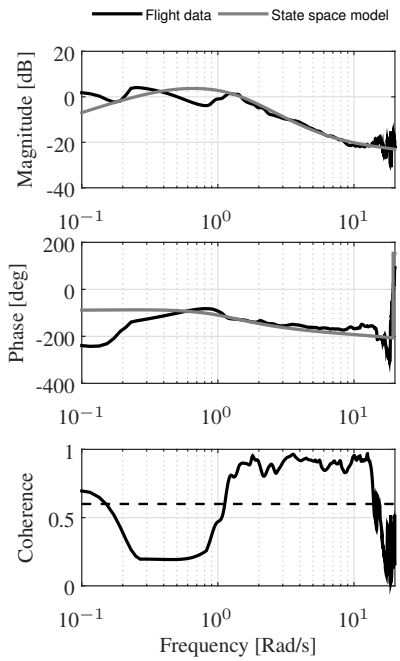

Fig. 16: Bode plot of state space model's of lateral acceleration to lateral cyclic input (a_y/δ_{lat}).

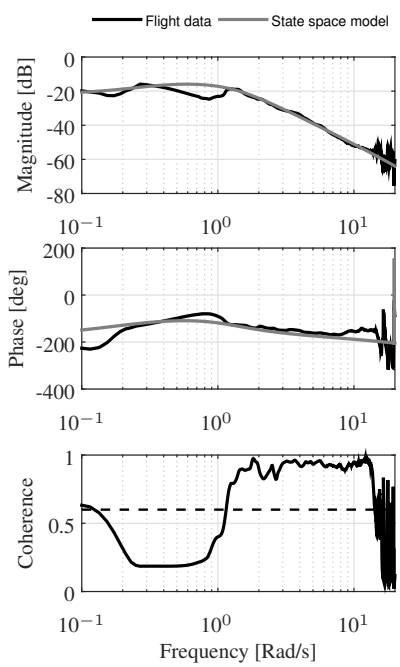

Fig. 17: Bode plot of state space model's roll angle to lateral cyclic input (ϕ/δ_{lat}).

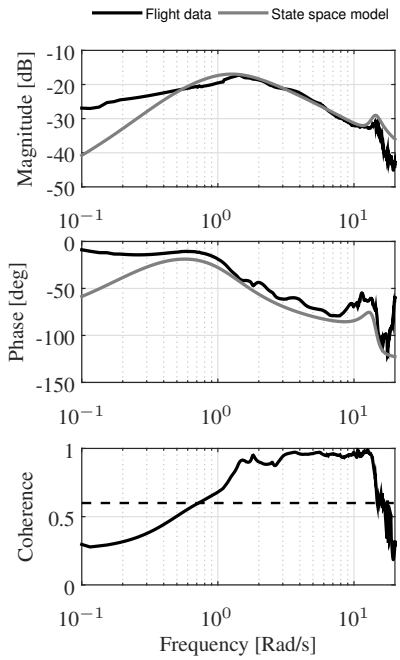

Fig. 18: Bode plot of state space model's roll-rate to lateral cyclic input (p/δ_{lat}).

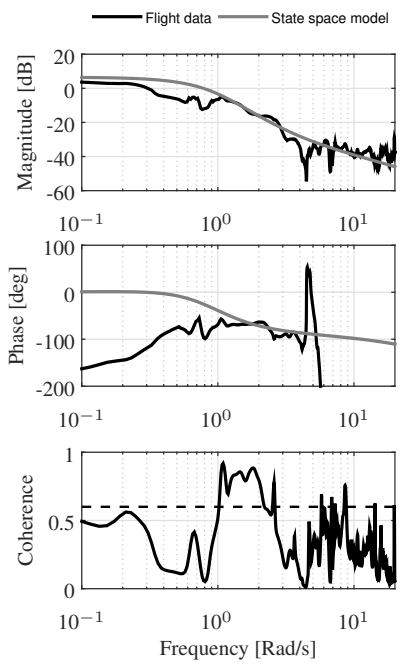

Fig. 19: Bode plot of state space model's longitudinal translational velocity to longitudinal cyclic input (u/δ_{lon}.)

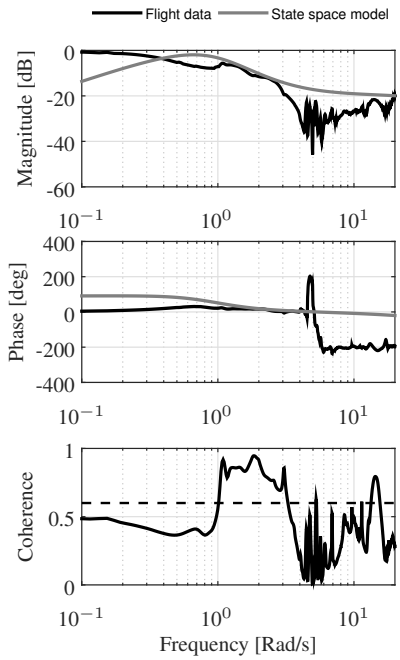

Fig. 20: Bode plot of state space model's longitudinal translational acceleration to longitudinal cyclic input (a_x/δ_{lon}).

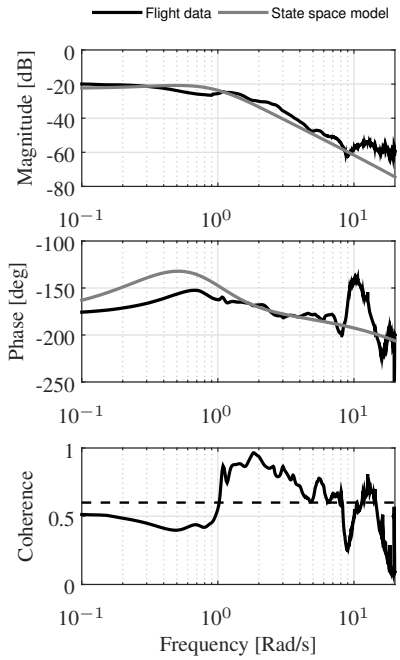

Fig. 21: Bode plot of state space model's pitch angle to longitudinal cyclic input (θ/δ_{lon}).

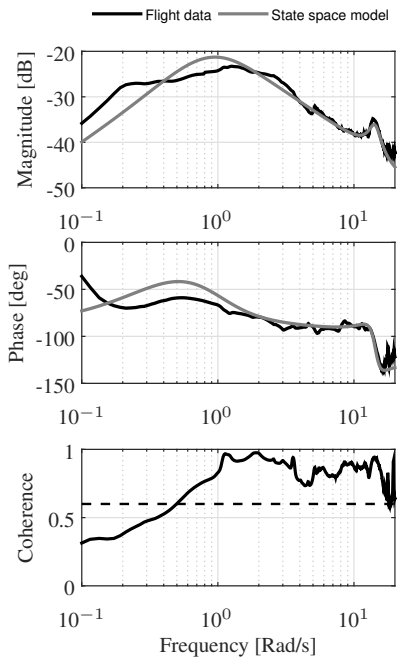

Fig. 22: Bode plot of state space model's pitch-rate to longitudinal cyclic input (q/δ_{lon}).

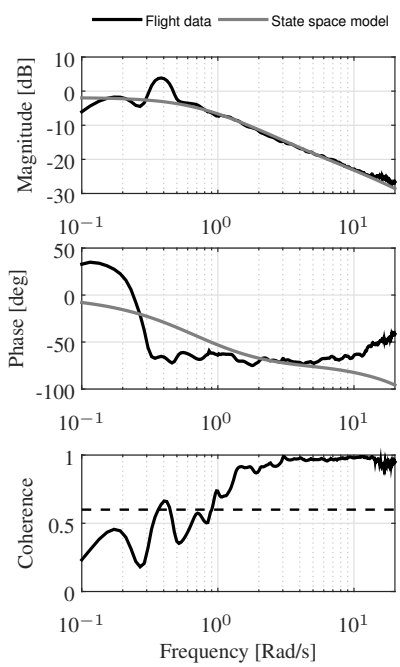

Fig. 23: Bode plot of state space model's translational vertical velocity to collective input (w/δ_{col}).

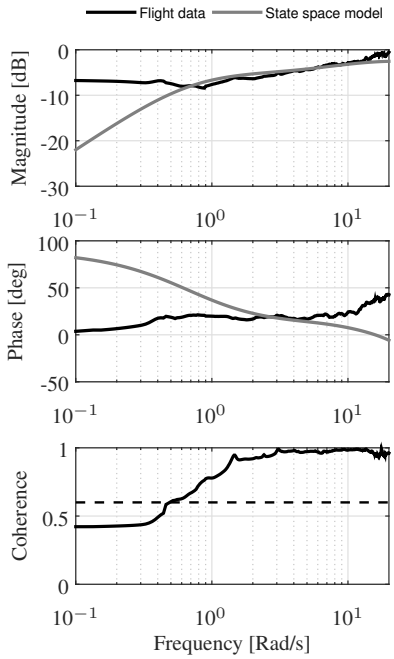

Fig. 24: Bode plot of state space model's vertical acceleration to collective input (a_z/δ_{col}).

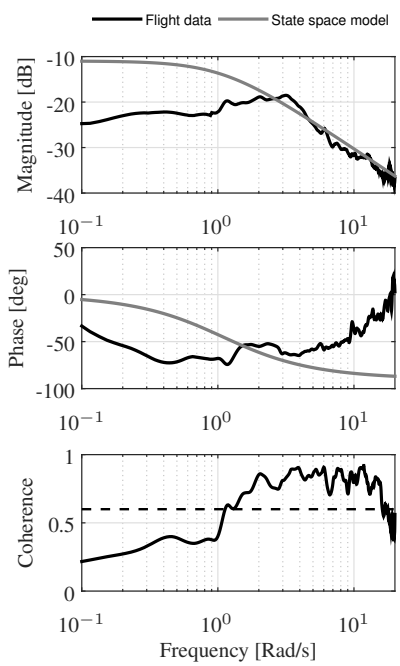

Fig. 25: Bode plot of state space model's yaw-rate to pedals input (r/δ_{ped}).